

Approved:

SPECTROSCOPIC ANALYSIS OF STARS IN THE
OUTSKIRTS OF NGC 1851

by

Tashveena Rani SURDHA

A THESIS SUBMITTED IN PARTIAL FULFILMENT OF
THE REQUIREMENTS FOR THE DEGREE OF

BACHELOR OF SCIENCE

in

Honours Astrophysics

(Department of Astronomy and Physics, Dr. Vincent Hénault-Brunet, supervising
faculty)

.....
.....
.....
.....
.....

SAINT MARY'S UNIVERSITY

May 11, 2021

© Tashveena Rani SURDHA, 2021

ABSTRACT

SPECTROSCOPIC ANALYSIS OF STARS IN THE OUTSKIRTS OF NGC 1851

by *Tashveena Rani SURDHA*

submitted on May 11, 2021:

NGC 1851 is a peculiar globular cluster with hints of a bimodal populations of stars (possibly two different episodes of formation of stars that resulted in a small spread in the metallicity in the centre of the cluster). It is suggested that it might have been part of a progenitor dwarf galaxy. Spectroscopic analysis of stars in the outskirts of this cluster can indicate its origin by looking at the metallicity distribution. The stars closer to the core of the cluster have a metallicity of $[\text{Fe}/\text{H}]=-1.18 \pm 0.2$ and the stars studied here are cluster members of NGC 1851 which are obtained based on Gaia DR2 parallaxes and proper motions and for which we have spectroscopic data from the FLAMES instrument on the Very Large Telescope covering a bigger area of the cluster, all the way to the Jacobi radius. The calcium infrared triplet lines, which are strong absorption lines in the range of 8400 Å to 9000 Å are investigated by looking at their equivalent width. The equivalent width, which is related to the metallicity of a star, is studied for 89 stars which are located in the outer regions of the cluster. Indication of a small spread in $[\text{Fe}/\text{H}]$ is found which might suggest that the cluster has not been part of a progenitor dwarf galaxy.

Contents

Contents	iii
List of Figures	v
1 Introduction	1
1.1 GLOBULAR CLUSTERS	1
1.2 DWARF GALAXIES	3
1.3 CALCIUM TRIPLET LINES (CAT)	4
1.4 NGC 1851	11
2 Data Structure and Reduction	15
2.1 OBSERVATIONS	15
2.2 DATA REDUCTION AND CALIBRATIONS	17
3 Methods for Spectroscopic Analysis	18
3.1 SKY SUBTRACTION	18
3.2 CONTINUUM FITTING	24
3.3 CAT LINES FITTING	26
3.4 EQUIVALENT WIDTHS	30
4 Results of the Spectroscopic Analysis	33

4.1	THE METALLICITY DISTRIBUTION	33
5	Discussion and Conclusion	35
5.1	THE SPREAD IN METALLICITY	35
	Bibliography	38

List of Figures

1.1	NGC 1851	2
1.2	The equivalent width (the width of the gray shaded area)	6
1.3	A CaT line (rest wavelength at 8542.09 Å) with the pseudo-Voigt profile.	6
1.4	The non-linear fitted calibration for the ΣCa of the two strongest CaT lines	9
1.5	The upper plot shows three polynomials of different degree fitted to the data. The lower plot shows three other calibrations fitted for the same metallicity scale and all four of them fitted for different metallicity scales	10
1.6	The colour-magnitude diagram of the bimodal population of NGC 1851. The green circle is the Jacobi radius	11
1.7	The spread in metallicity for stars in the halo and the centre of the cluster NGC 1851	14
2.1	Distribution of the stars targeted with FLAMES in NGC 1851. The red circle is the Jacobi radius, the blue circle is the King radius and the green circle is the half-light radius.	16
3.1	The spectrum of a star with prominent sky emission lines present. . .	19

3.2	The spectrum of the closest sky fibre.	19
3.3	The subtraction of the closest sky spectrum from a star spectrum. . .	20
3.4	The median of the spectra of a few sky fibres closest to the star position	21
3.5	The subtraction of the median of the few closest sky spectra from a star spectrum.	22
3.6	The median of all the sky fibres spectra.	23
3.7	The subtraction of the median of all the sky fibres from the star spectrum.	23
3.8	The spectrum of one of the sample stars (in purple) with masked CaT lines (in pink) and the subtraction of the median of all the sky fibres from the star spectrum. The wavelength is heliocentric corrected. . .	24
3.9	The continuum fitting of a spectrum is shown as the green dashed line. The CaT lines are masked when fitting the continuum.	25
3.10	Fit of the CaT lines with a pseudo-Voigt profile for one of the sample stars.	29
3.11	The poorly fitted pseudo-Voigt profile for a star using MCMC. . . .	30
4.1	The metallicity distribution of the stars in the outskirts of NGC 1851 studied in this thesis (blue histogram). The orange Gaussian distribu- tion represents the [Fe/H] distribution if the stars had no significant metallicity spread and the same metallicity as the stars in the centre of the cluster.	34
5.1	The line-of-sight velocity distribution with [Fe/H] of the stars.	36

Chapter 1

Introduction

1.1 GLOBULAR CLUSTERS

A globular cluster is a roughly spherical system of stars that are bound gravitationally within a certain radius as shown in Figure 1.1. The number of stars in a globular cluster ranges from about a hundred thousands to millions. Globular clusters are usually spherical with a half-mass radius of around a few pc (Harris, 1996(updated 2010 Edition)). In the Milky Way galaxy, there are 157 globular clusters that are classified in the catalogue of Harris (1996) (updated 2010 Edition) which contains the basic parameters of the globular clusters. Globular clusters can be formed in the main galaxy in which they currently reside, or form around a satellite galaxy that is then accreted by the main galaxy. Some globular clusters are also thought to be the leftover nuclear star cluster of a dwarf galaxy that was disrupted after being accreted (e.g. Marino, 2014). Globular clusters normally contain stars that have the same metallicity since they are formed in the same chemical environment, that is in the same molecular clouds. Photometric studies of globular clusters in different massive galaxies have shown that globular clusters display a bimodal colour distribution which means that there are two different populations of globular clusters: the metal-poor

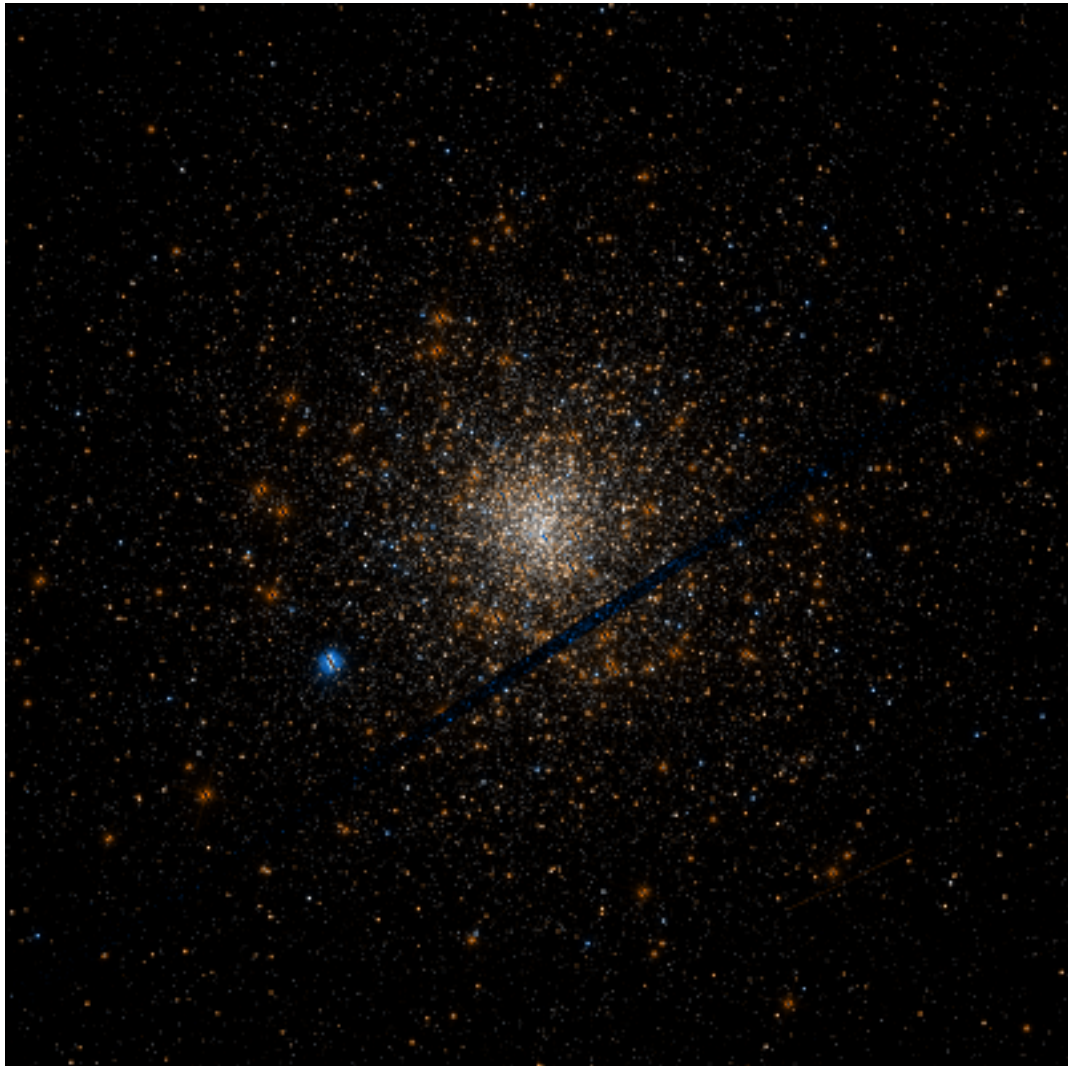


Figure 1.1: NGC 1851 (Credit: NASA, ESA, and The Hubble Heritage Team (STScI/AURA))

globular clusters and the metal-rich globular clusters. Metal-poor globular clusters are thought to be formed in the early universe, in the dark matter halo of galaxies and the metal-rich globular clusters are born in the disc of galaxies formed by gas dissipation in the early universe (Brodie & Strader, 2006). Brodie & Strader (2006) also explains why metal-rich clusters are found to be around 20% larger than metal-rich clusters (Kundu & Whitmore, 1998).

Globular clusters normally consist of stars bounded inside the King radius beyond

which the number density of stars goes almost to zero (King, 1962). Stars that are within a few half-light radii from the cluster core are still considered to be gravitationally bound to the cluster and found within the King radius. The Jacobi radius is the distance from the globular cluster centre where a star is no longer gravitationally bound to the cluster. The Jacobi radius may vary in different globular clusters depending on their orbital eccentricity around the Milky Way galaxy. The tidal pull on a globular cluster depends on where the latter is found from the Galactic centre hence affecting its Jacobi radius which is also known as the tidal radius. At the King radius, the density of stars drops drastically but it is possible to find stars beyond the King radius and within the Jacobi radius.

1.2 DWARF GALAXIES

Most galaxies found near the Milky Way galaxy are dwarf galaxies. McConnachie (2011) has classified the Local Group galaxies with absolute visual magnitude larger than -18 as dwarf galaxies. Two well-known dwarf galaxies that orbit the Milky Way galaxy are the Large Magellanic Cloud and the Small Magellanic Cloud. Dwarf galaxies have a low surface brightness and contain dark matter which makes them interesting to study (Gallagher et al., 1994). Rusakov et al. (2021) found that there are more star formation events in the centre of the Fornax dwarf galaxy and Mercado et al. (2021) found that the central regions of 10 observed dwarf galaxies along with 28 simulated dwarf galaxies, have a larger metallicity than the periphery showing that the stars in the dwarf galaxies are not all formed at the same time and with the same

material due to extended star formation period. The central region of a dwarf galaxy has a higher surface brightness than the outer region. The origin of dwarf galaxies is still under debate and a lot is still unknown about them. Due to tidal interactions with the Milky Way galaxy or other substructures, dwarf galaxies can be completely disrupted or the outer parts of the dwarf galaxies can be stripped off of their stellar content and the nuclear star cluster left behind is thought to be the origin of certain globular clusters such as ω Centauri (Bekki & Freeman, 2003).

1.3 CALCIUM TRIPLET LINES (CAT)

Understanding the metallicity distribution of a system is important as it tells us about the environment in which it was formed and it helps in distinguishing the stars of a globular cluster which are formed in the same environment at the same time and the stars of a dwarf galaxy which have formed in different environment due to extended star formation period. Metallicity is the abundance of metals compared to lighter elements such as hydrogen and helium and is often denoted as $[Z/H]$ which is the logarithmic value of the number density ratio of elements Z and H as compared to the Sun, where Z is an element heavier than hydrogen and helium. In astronomy and physics, the most common tracer for metallicity used is the abundance of iron (Fe) because it is easy to measure the several Fe lines found in a spectrum and also the abundances of other metals is assumed to change in proportion to the change in the abundance of Fe. The metallicity, $[Fe/H]$ is the logarithmic value of the ratio of the number density of the elements Fe and H in the star as compared to the Sun.

The measurement of metallicity is mostly used to study the composition of a star and the atmospheric composition of planets and exoplanets. The metallicity of a star depends on how much metal polluted the star formation site is and hence can tell us about the environment before it was formed. Although the iron lines can be used to determine the metallicity of main sequence stars and red giants, calcium triplet lines (CaT lines) are better to use for the spectroscopic study of red giants in the infrared regime. CaT lines can be used to infer the iron abundances too. The CaT lines have rest wavelengths at 8498.02 Å , 8542.09 Å and 8662.14 Å (e.g. Wan et al, 2021). In the same wavelength regime, there are weaker lines such as the Fe I and Ti I lines which begins to appear in cooler stars. There are other weaker lines such as TiO and VO which gets stronger in cooler stars. To measure the strength of CaT lines, the equivalent width of the line is calculated. The equivalent width is defined as the area between the absorption line and the continuum level (with the continuum intensity normalized to 1), and can be visualized as the width of the shaded grey area in Figure 1.2.

The continuum level (the flux in between spectral lines) can be found by fitting with a polynomial while masking the important and strong absorption lines. The CaT lines are usually fitted with the sum of a Gaussian function, and a Lorentzian function which accounts for the wings of the line profile (a pseudo-Voigt profile; Carrera et al., 2007) as shown in Figure 1.3. The equivalent widths of the CaT lines are added to give the CaT index which is denoted by ΣCa . Since the strength of the absorption lines also depends on the effective temperature and surface gravity of the stars (not just on the abundance), these effects must be removed so that the effect of abundance

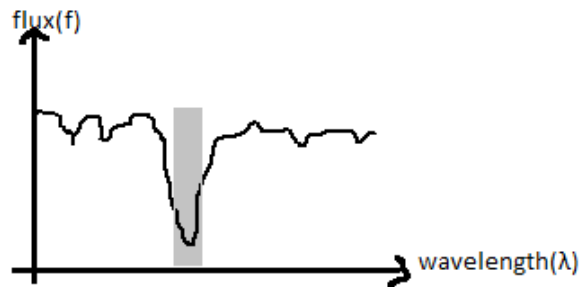


Figure 1.2: The equivalent width (the width of the gray shaded area)

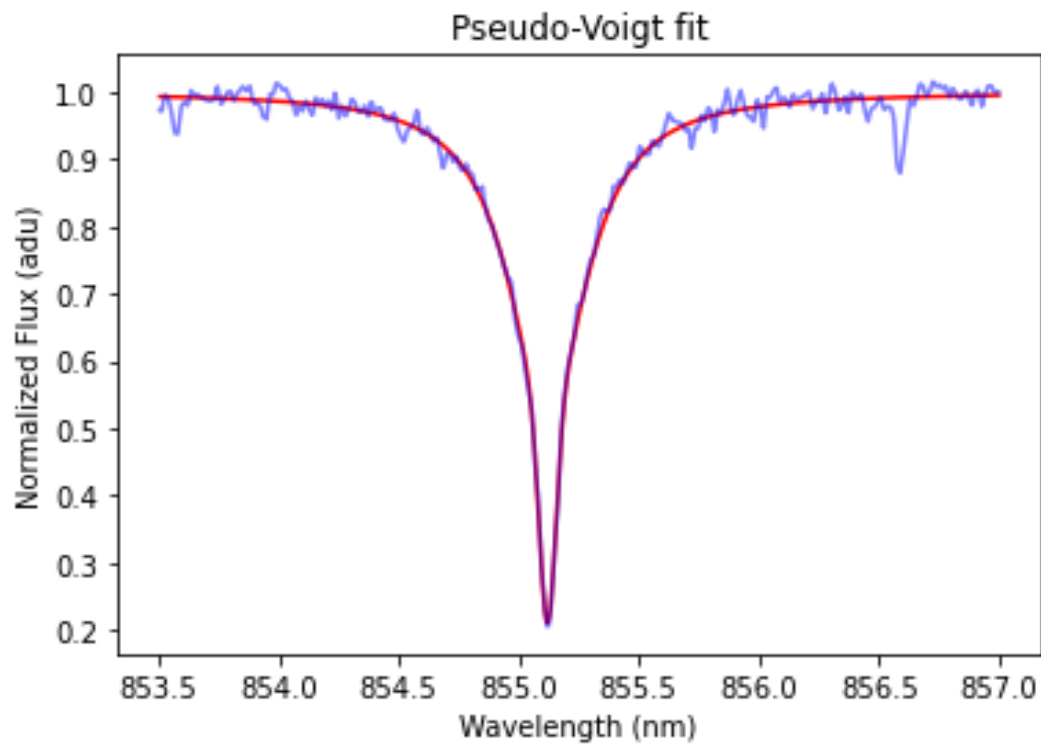


Figure 1.3: A CaT line (rest wavelength at 8542.09 \AA) with the pseudo-Voigt profile.

is isolated and the metallicity can be found. Therefore the luminosity- ΣCa plane is used as described by Armandroff & Da Costa (1991). Rutledge et al. (1997b) found

that the slope of the $\Sigma\text{Ca}-(V-V_{HB})$ line in the luminosity- ΣCa plane is the same for all the clusters regardless of their metallicities but the plane intercept with the ΣCa axis changes and it is defined as the reduced equivalent width (Carrera et al., 2007). This implies that the reduced equivalent width changes with the metallicity. Carrera et al. (2007) describes the luminosity- ΣCa plane by equation 1.1:

$$\Sigma\text{Ca} = W'_{HB} + \beta(V - V_{HB}), \quad (1.1)$$

where W'_{HB} is the reduced equivalent width, V is the visual magnitude and V_{HB} is the visual magnitude of the horizontal branch of the cluster, and β is the slope of line in the luminosity- ΣCa plane. ΣCa is measured during the spectroscopic analysis as discussed in 3.4 and W'_{HB} is calculated.

Three metallicity scales were compared with metallicities obtained by fitting the spectrum for stars in open clusters. With the metallicity scale of Carretta & Gratton (1997) which is obtained with high-resolution spectroscopy, Carrera et al. (2007) found a linear correlation between metallicity $[\text{Fe}/\text{H}]$ and the reduced equivalent width. Another linear correlation between $[\text{Fe}/\text{H}]$ and the reduced equivalent width was found using the Kraft & Ivans (2003) metallicity scale which is also obtained from high-resolution spectroscopy. A second-order polynomial relation was found using the Zinn & West (1984) metallicity scale obtained using low-resolution spectroscopy. The metallicity scales obtained from high-resolution spectroscopy are good to use for both open clusters and globular clusters. However, a non-linear relationship was found between $[\text{Fe}/\text{H}]$ and W'_{HB} using the Armandroff & Da Costa (1991) metallicity scale

by Carretta & Gratton (1997) since their study used a poor fit for the CaT lines (Gaussian fitting only). Hence, the CaT index found was different and affected the relationship between $[\text{Fe}/\text{H}]$ and W'_{HB} . There was an underestimate of the metallicity therefore, if the metallicity scale is non-linear and the CaT lines are poorly fitted, it affects the metallicity. So, the metallicity varies linearly with W'_{HB} (Carrera et al., 2007).

However, Husser et al. (2020) used a non-linear calibration for the reduced equivalent width as shown in Equation 1.2 which accounts for stars fainter than the horizontal branch, for which it is more difficult to fit the CaT lines.

$$W' = \Sigma Ca + 0.442 \cdot (V - V_{HB}) - 0.058 \cdot (V - V_{HB})^2, \quad (1.2)$$

Figure 1.4 shows the fitting of the non-linear equation for W' for all red-giant branch (RGB) stars and the ΣCa used is the sum of the two strongest absorption lines. The blue line shows a linear relation fitted for stars brighter than the horizontal branch.

A non-linear metallicity scale was found (Husser et al., 2020) as shown in Figure 1.5 and it is given by Equation 1.3:

$$[\text{Fe}/\text{H}] = -2.52 - 0.04 \cdot W' + 0.07 \cdot (W')^2 \quad (1.3)$$

This work will use the summation of the equivalent widths of the two strongest CaT lines for the calibration of ΣCa and the non-linear relationship between $[\text{Fe}/\text{H}]$ and W' by Husser et al. (2020).

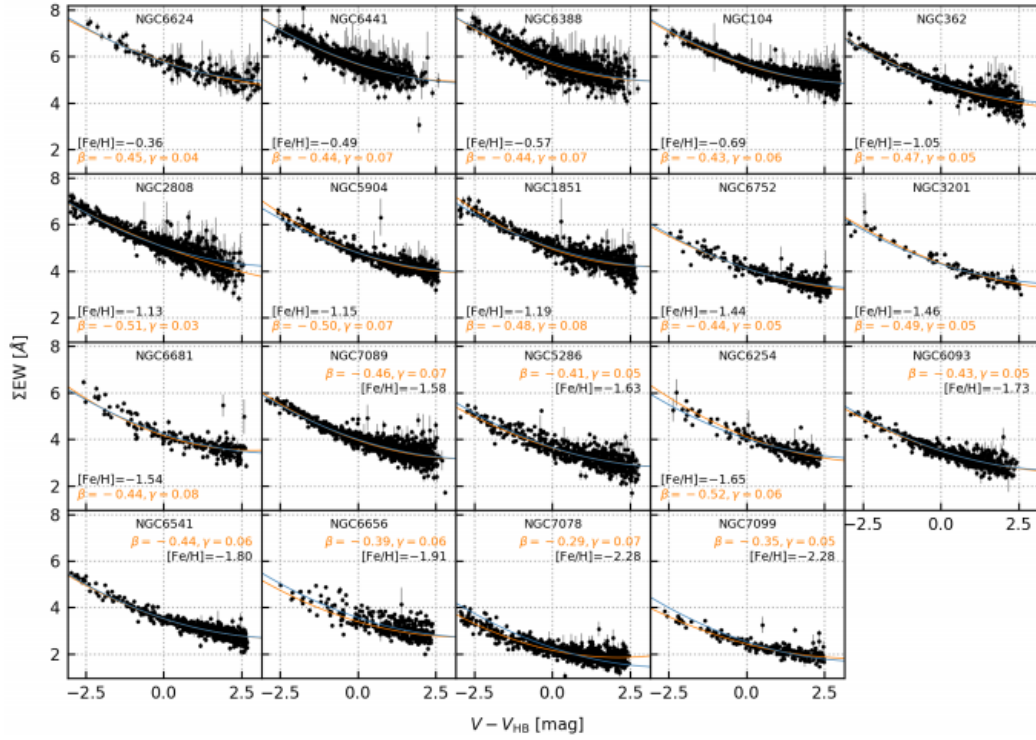


Figure 1.4: The non-linear fitted calibration for the ΣCa of the two strongest CaT lines. (Credit: Husser et al. (2020))

Ground-based telescopes must correct for the sky emission lines which will affect both the continuum level and the fitting of the CaT lines. The spectroscopic analysis of a star can also tell us about its radial velocity. The radial (i.e. line-of-sight) motion of a star shifts the entire spectrum along the wavelength axis and the Doppler shift which is given by the equation 1.4 below is used to calculate the radial velocity of the star:

$$\frac{v}{c} = \frac{\Delta\lambda}{\lambda} \quad (1.4)$$

where v is the radial velocity of the star; c is the speed of light; $\Delta\lambda$ is the shift in wavelength; λ is the rest wavelength of a transition in vacuum. It is to be noted that

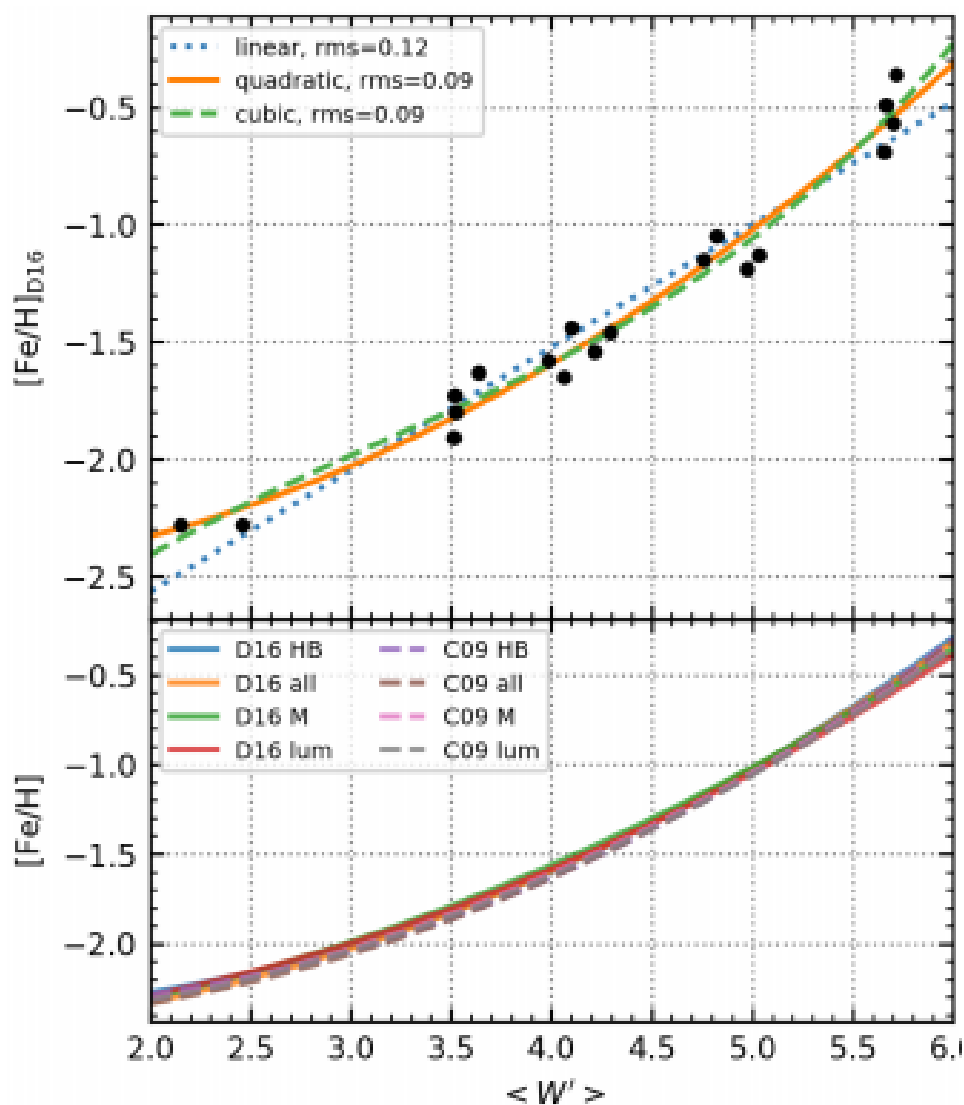


Figure 1.5: The upper plot shows three polynomials of different degree fitted to the data. The lower plot shows three other calibrations fitted for the same metallicity scale and all four of them fitted for different metallicity scales. (Credit: Husser et al. (2020))

the motion of the Earth around the Sun (heliocentric motion) must be corrected as it will also shift the spectrum. The velocity will help in determining which star is a member of the cluster. Stars with velocity similar to the cluster will be considered cluster members while those with velocity varying significantly from the cluster radial velocity will not be considered for analysis of the metallicity distribution.

1.4 NGC 1851

NGC 1851 is a peculiar globular cluster because it has an extended stellar envelope (Marino et al., 2014) and a stellar stream (Sollima et al., 2012). There are cluster stars within its Jacobi radius but outside the King truncation radius (Carballo-Bello et al., 2012).

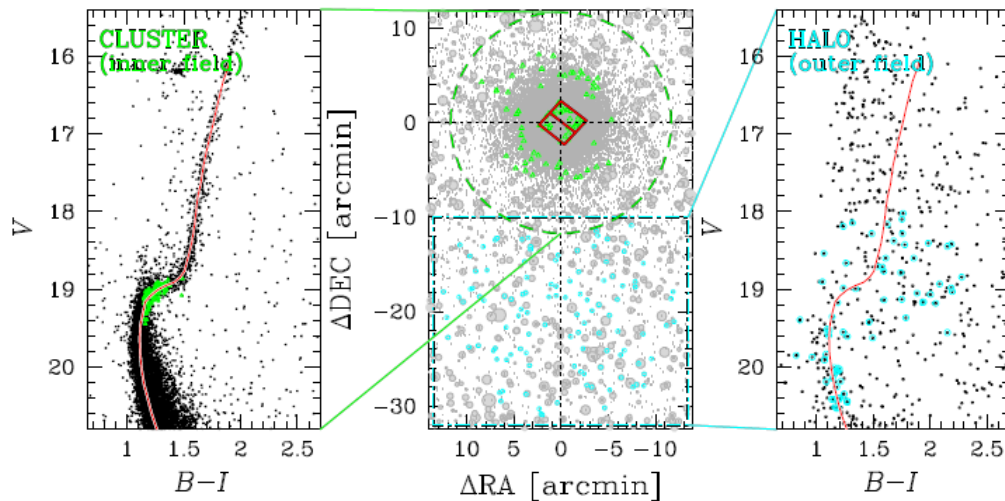


Figure 1.6: The colour-magnitude diagram of the bimodal population of NGC 1851. The green circle is the Jacobi radius. (Credit: Marino et al. (2014))

The diffuse stellar halo (with a radius more than 250 pc from the cluster centre) extends beyond the King radius of the cluster which is around 11.7 arcmin (Harris, 1998 (updated version 2010)) but is within the Jacobi radius and contains stars that show radial velocities and metallicities similar to stars within the Jacobi radius (Marino et al., 2014), however the study of Marino et al. (2014) was based on a statistically small number of stars (15 stars out of the 23 stars they studied). NGC 1851 shows the presence of two subgiant branches (Han et al., 2009) which suggests that the globular cluster might have been formed from the merging of two different

globular clusters (Marino et al., 2014). Figure 1.7 shows the bimodal population of NGC 1851. The stellar envelope suggests that the cluster could have been formed from a progenitor dwarf galaxy like the globular cluster, ω Centauri (Bekki & Freeman, 2003). ω Centauri is considered to be the nucleus of a dwarf galaxy that has been disrupted by tidal interactions with the Milky Way. Its internal metallicity variation suggests that it had the same mass as small galaxies which could retain fast supernova ejecta (Marino et al., 2014). The resemblance of NGC 1851 to ω Centauri in terms of mass, suggests that it may have also been part of a dwarf galaxy.

One scenario for the formation of NGC 1851 is that there were two globular clusters that have merged in together forming the two subgiant branches observed now and this event has occurred in a dwarf galaxy. The dwarf galaxy was tidally stripped of its stars by the Milky Way leaving behind the newly formed globular cluster (Marino et al., 2014). Hence the stellar halo around NGC 1851 would contain stars from the progenitor galaxy and the central regions of the cluster would contain stars from the two merged globular clusters. The merging of the two globular clusters would explain the two different subgiant branches but it does not explain the stellar envelope which can possibly explain the scenario of it being from a progenitor dwarf galaxy although it is not necessary that the cluster is a product of the merging of two clusters. If the cluster was formed from a progenitor dwarf galaxy then it would contain stars with different stellar generations and a broader spread in metallicity unless the metallicities of one of the merged globular clusters and the progenitor galaxy are the same (Bekki & Yong, 2012). The stellar envelope might also be explained by the tidal effect of the Milky Way alone, which would give rise to "potential escapers" (Kupper et al.,

2010, Claydon et al., 2017) which are stars that are energetically unbound but that have not yet escaped the cluster, and that are found beyond 0.5 times the Jacobi radius. If NGC 1851 was formed as part of a dwarf galaxy, the implication would be that all globular clusters are not formed in the same way and it will contribute to the ‘missing’ satellites problem of the Λ cold dark matter (Marino et al., 2014).

It has been suggested the NGC 1851 was part of the Canis Major (CMa) dwarf galaxy (Forbes & Bridges 2010) and there can be a spread in metallicity as in a debris scenario. Figure 1.7 shows the metallicity distribution of stars in the halo and the center of the cluster NGC 1851 for a small sample of stars. The metallicity analysis for the study conducted by Marino et al. (2014) was done for a low resolution. There was no spread in the metallicity in their halo sample, but it was expected because they preferentially observed a sample of first population stars. The focus of this thesis will be on a larger sample of stars found in the outer regions of the cluster at high resolution. With proper motion and parallaxes from Gaia now available, efficient selection of member stars in the outskirts of globular clusters is now possible. Whereas before it was very difficult to target those stars because of large numbers of contaminants in the cluster outskirts, these contaminants can be identified and removed using Gaia data. This enabled the selection of a large number of member stars in the outskirts which were followed by spectroscopically with the FLAMES multi-object spectrograph on the Very Large Telescope (VLT), and the analysis of these FLAMES spectra for NGC 1851 is presented in this thesis. If a large spread in metallicity is found, this will suggest that NGC 1851 was part of a progenitor dwarf galaxy. A small spread would suggest otherwise and will be more likely to explain a

scenario of potential escapers for which the line-of-sight velocity has to be studied.

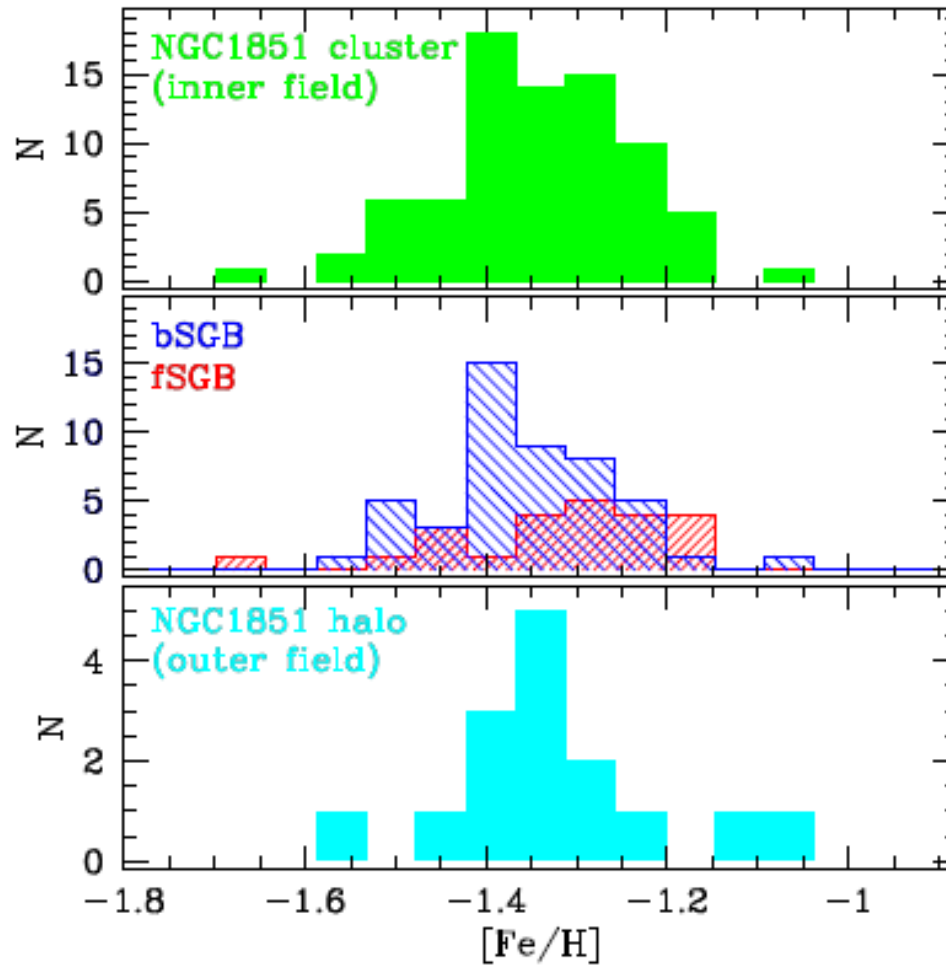


Figure 1.7: The spread in metallicity for stars in the halo and the centre of the cluster NGC 1851. (Credit: Marino et al. (2014))

Chapter 2

Data Structure and Reduction

2.1 OBSERVATIONS

For this study, data from the FLAMES/GIRAFFE spectrograph was used which is located at the Very Large Telescope (VLT) in Chile. The GIRAFFE spectroscopy uses a high-resolution grating, HR21, which allows the observation of the CaT lines, which will be useful to infer the metallicity of individual stars as described in Section 1.3. FLAMES can obtain spectra of more than a hundred objects within a field of view of 25 arcminutes in diameter. The observations were obtained as part of a spectroscopic survey of three globular clusters (ESO Program ID 0102.D-0164(A)) but we focus in this thesis on the analysis of data for NGC 1851 only. In planning this spectroscopic survey, the second Gaia data release (GDR2) allowed the selection of member stars for spectroscopic follow-up from background and foreground stars using proper motions and parallaxes.

For NGC 1851, two FLAMES fields were observed at two different locations close to the Jacobi radius, on two opposite sides of the cluster centre. Separate observations were also performed at two different times of the year (around a month apart). Spectroscopic data of the stars were obtained twice for the two different locations, that is, a star member was observed twice in an interval of a month and there are

now four observing blocks. This procedure allows the identification of binaries, that is, through the spectroscopic analysis, if the two observations of the same object result in two different velocities that are not compatible within uncertainties, then the object may be assumed to be a binary and can thus be removed for further analysis of the velocity distribution for the stars in the outskirts of this cluster. A total of 221 spectroscopic observations including background sky observations were obtained from FLAMES for NGC 1851 (The number of observations of the stars was 213, excluding sky observations). The distribution of the target positions in NGC 1851 for both epochs is shown in Figure 2.1.

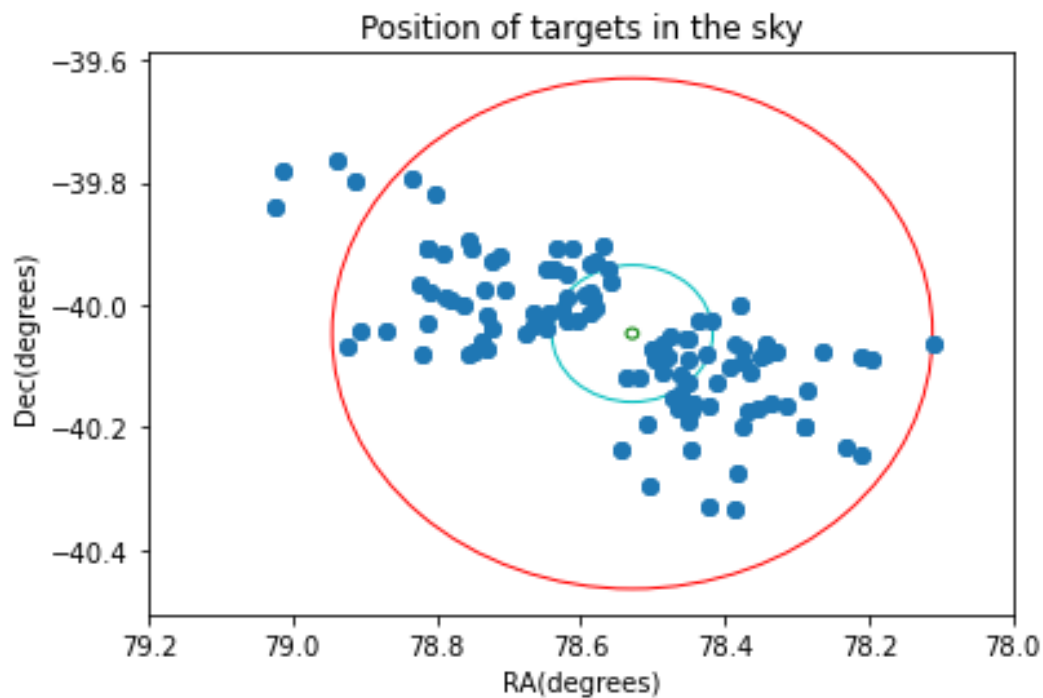


Figure 2.1: Distribution of the stars targeted with FLAMES in NGC 1851. The red circle is the Jacobi radius, the blue circle is the King radius and the green circle is the half-light radius.

After downloading the data for all three clusters observed as part of the same program, the data for the cluster NGC 1851 which is being studied in this thesis

is sorted out by finding the files for the stars observed within 1.5 degrees from the centre of the cluster. The Right Ascension and Declination of the cluster centre are $05^h14^m06.76^s$ and -40.05° (Harris, 1996(updated 2010 Edition)).

2.2 DATA REDUCTION AND CALIBRATIONS

The spectroscopic data obtained from FLAMES was already reduced and calibrated by pipeline processing of the GIRAFFE instrument (version giraf-2.16.3) by the Quality Control Group of the European Southern Observatory. The data was pre-processed to remove cosmic rays and then it was pipeline-processed which consists of bias correction, masking of bad pixels, residual wavelength drift derivation, heliocentric, barycentric and geocentric corrections, dark and flat calibrations and wavelength calibration.

The observations were also done by placing sky fibres together with fibres to observe the stars. For each epoch, around 19-20 sky fibres have been used and their spectroscopic data were processed by the GIRAFFE pipeline and stored in one fits file with observation epoch corresponding to the observing block. The sky subtraction of the stars' spectroscopic data was not done as part of the pipeline processing so that there is freedom in the method of sky subtraction using the sky fibres data, i.e. to find the best method to subtract the sky emission lines. The sky subtraction should be done by correcting back the heliocentric correction which was done to account for the movement of the Earth around the Sun which would otherwise cause a Doppler shift in the absorption lines of the stars, introducing errors in the radial velocity derived.

Chapter 3

Methods for Spectroscopic Analysis

3.1 SKY SUBTRACTION

The processed data contains sky emission lines since they were not subtracted during the standard calibration and reduction of the data, for the convenience of the user who can then apply the sky subtraction method most appropriate for their dataset. The spectroscopic data of the stars have been heliocentric corrected whereas the spectroscopic data of the sky fibres have not been heliocentric corrected. This implies that the spectroscopic data of the stars are shifted slightly in wavelength compared to the spectroscopic data of the sky. To do the sky emission lines subtraction from the star spectrum, it is important to get an alignment of the sky spectrum with the star spectrum. The heliocentric velocity correction is provided for each star. Using Equation 1.4, the star spectrum is heliocentric uncorrected. The sky spectrum now aligns with the star spectrum and can be subtracted with the procedure below.

For each observing block, the number of fibres placed on stars is between 53 and 56. The first sky subtraction procedure tested consisted of taking the closest sky fibre from the star by looking at the angular distance which is the smallest between the star fibre and sky fibre. The spectrum from the closest sky fibre is subtracted from

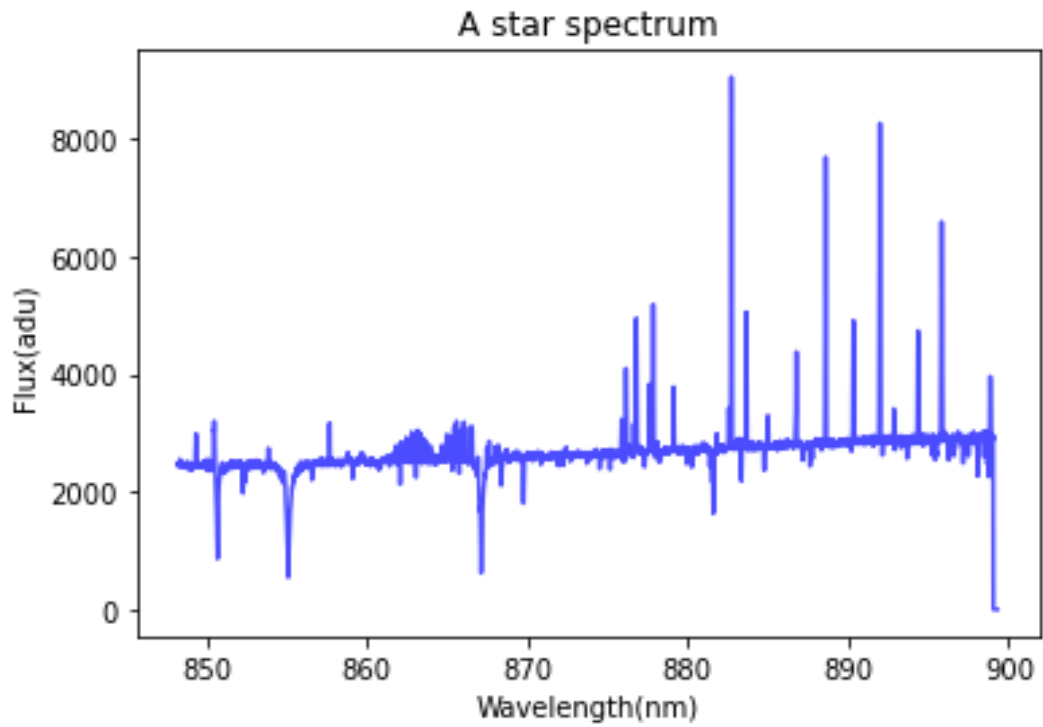


Figure 3.1: The spectrum of a star with prominent sky emission lines present.

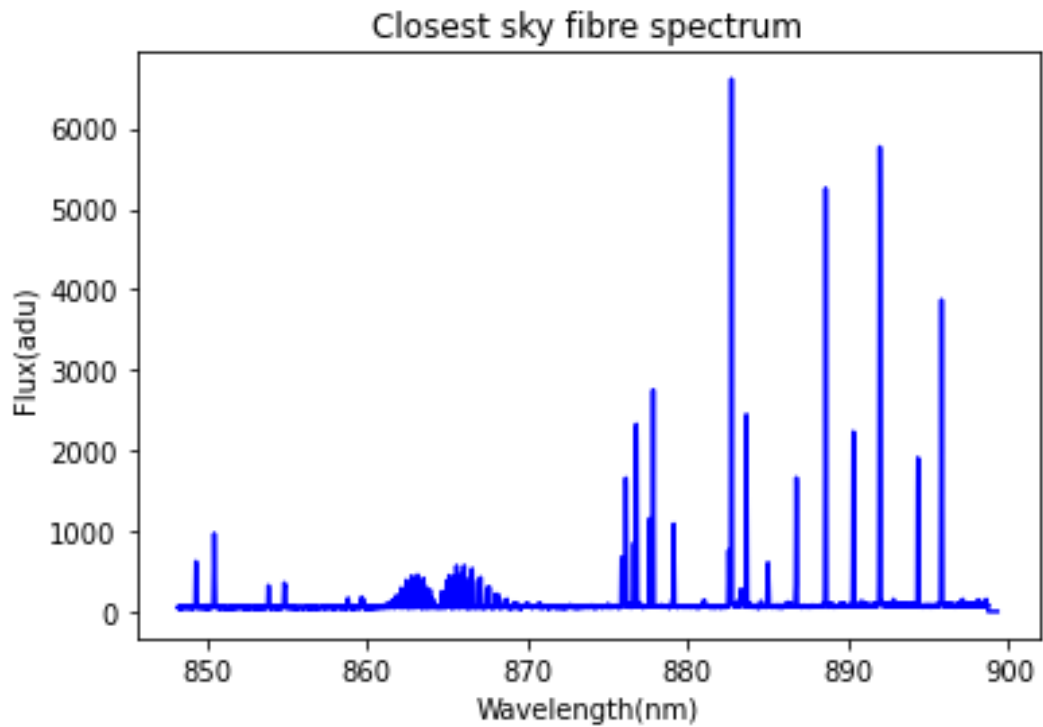


Figure 3.2: The spectrum of the closest sky fibre.

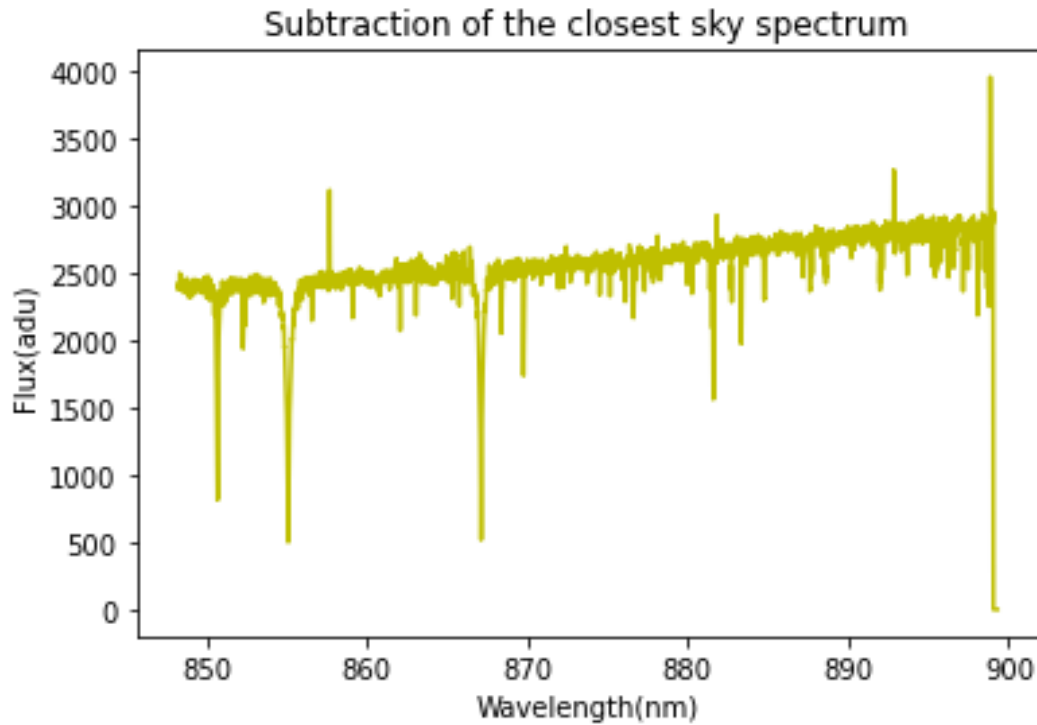


Figure 3.3: The subtraction of the closest sky spectrum from a star spectrum.

the spectrum of the star. An example resulting spectrum for one of the stars in the sample is shown in Figure 3.3. The sky spectrum for the closest fibre is shown in Figure 3.2 and the star spectrum before the sky subtraction is shown in Figure 3.1. The presence of strong emission lines is still seen in Figure 3.3.

To optimise subtraction of the sky emission lines, another method was tested. From the 19 to 20 sky fibres, those closest to a star are found by finding the angular separation between the star fibre and the sky fibre. Then the sky fibres with angular separations less than the minimum angular distance plus 0.07° are considered. A median spectrum of the few sky fibres is calculated and subtracted from the stars' spectra for the corresponding observing block. Figure 3.4 shows the median of the sky spectra of a few closest sky fibres. The resulting sky subtraction data is shown in

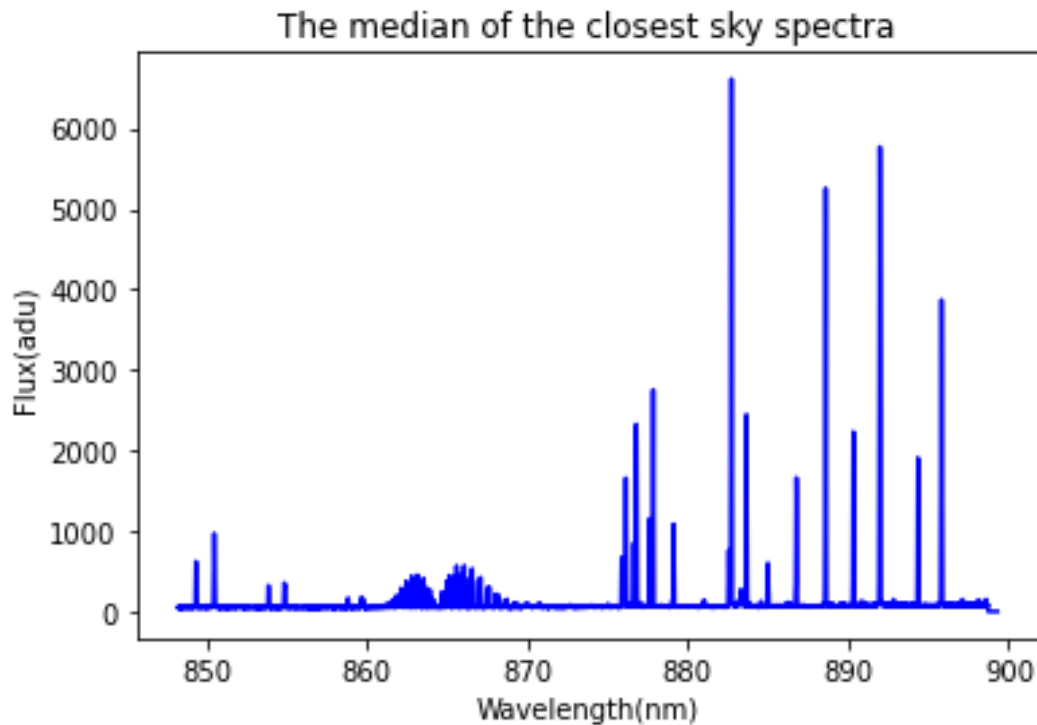


Figure 3.4: The median of the spectra of a few sky fibres closest to the star position

Figure 3.5. As seen in Figure 3.5, the emission lines are still present. Another method was also attempted by subtracting the median of the spectra of all the sky fibres from the spectrum data of the star. Figure 3.6 shows the spectrum obtained after doing a median of all the sky fibres spectra for one observing block. The resulting spectrum is shown in Figure 3.7 and the sky emission lines presence appears to be similar to the method of subtracting the median of the few closest sky fibres. Another procedure would be to take the mean of all the sky spectra, however this method is more sensitive to outliers among the sky spectra. This might result in over subtracting or under subtracting the sky spectra or inaccurate subtraction of the sky spectra.

The method of doing the median of all the sky spectra and subtracting it from the star spectrum is the preferred method used in this thesis although some sky

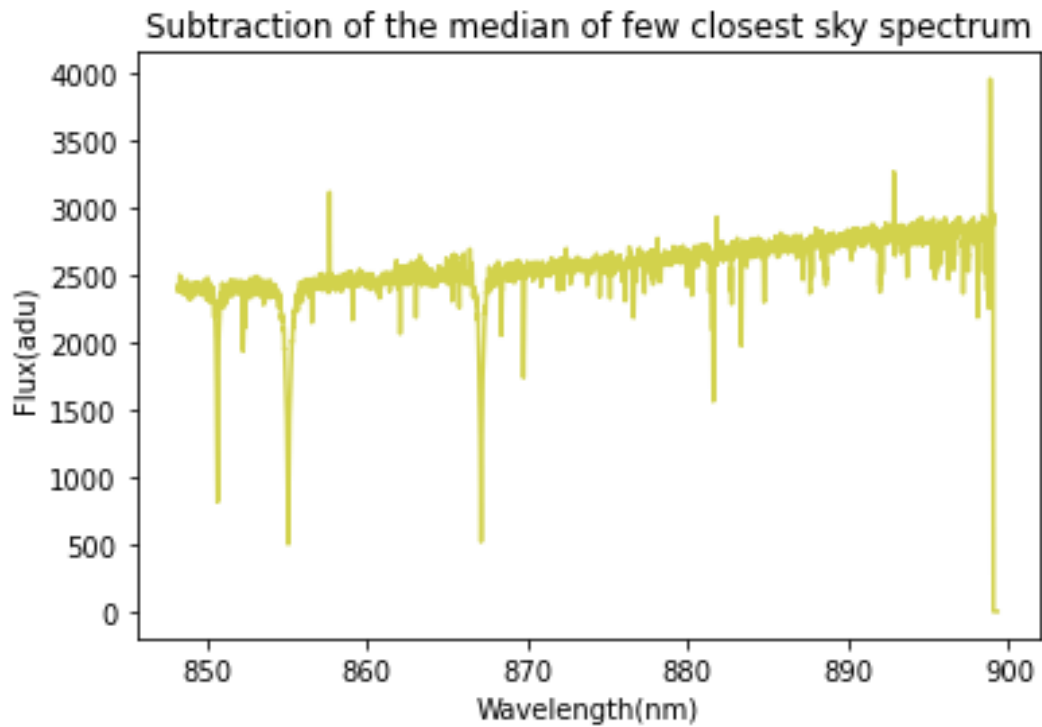


Figure 3.5: The subtraction of the median of the few closest sky spectra from a star spectrum.

emission lines artifacts are still present, mostly at the longer wavelengths of the spectrum as shown in Figure 3.7. The presence of the emission lines could affect the continuum fitting as discussed in Section 3.2 so it is important to remove them as much as possible. After sky subtraction, the wavelengths are corrected back again for heliocentricity.

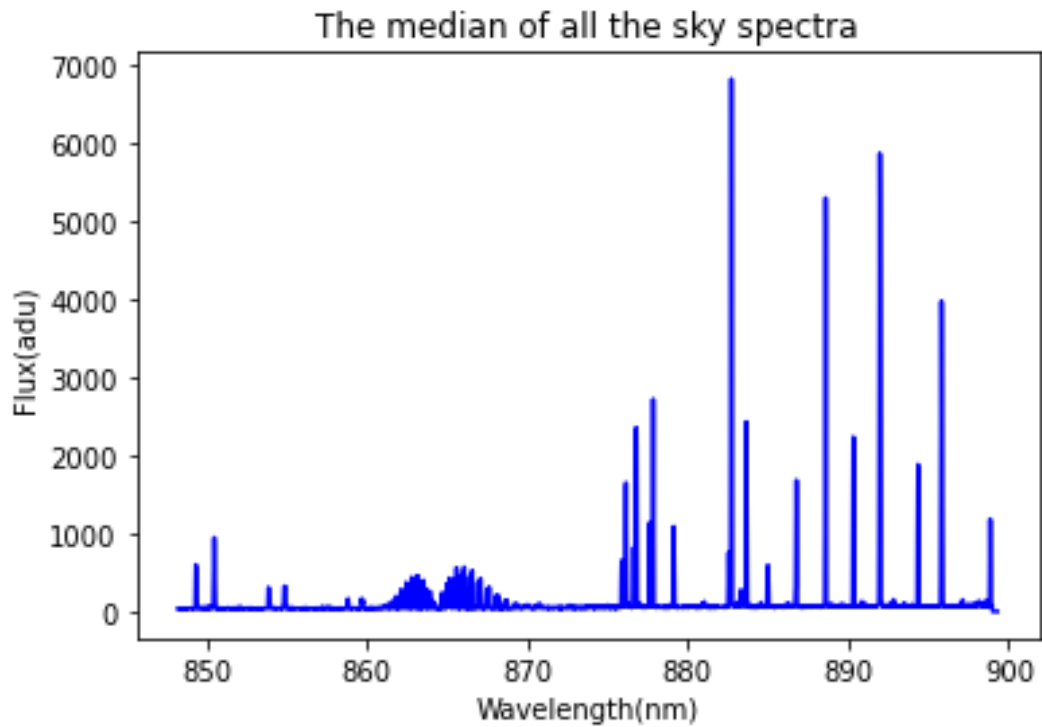


Figure 3.6: The median of all the sky fibres spectra.

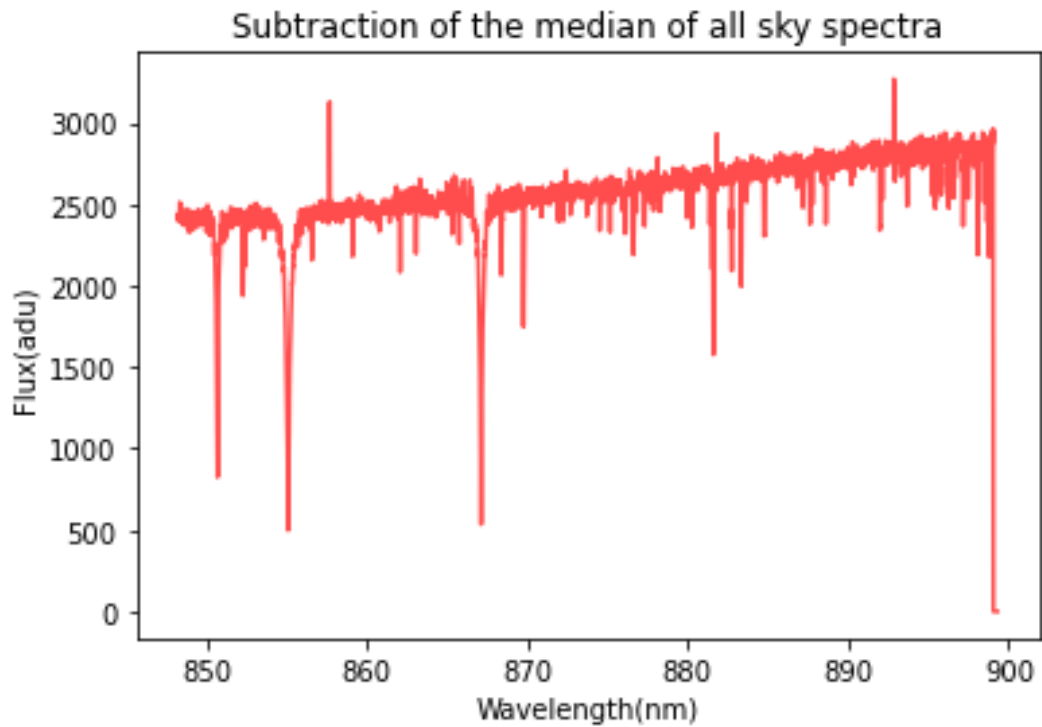


Figure 3.7: The subtraction of the median of all the sky fibres from the star spectrum.

3.2 CONTINUUM FITTING

To do the continuum fitting, the strong absorption lines must be masked so as to avoid an underestimation of the continuum. For this bandpass of 8400 Å to 9000 Å the strongest absorption lines are the CaT lines, so they have been masked to do the continuum fitting. The fluxes over the CaT lines regions are masked ensuring that they also include the regions of the wings of CaT lines. The masked regions are 8500 Å to 8514 Å ; 8538 Å to 8562 Å and 8661 Å to 8683.4 Å and they cover the extent of the CaT lines for all the stars in our sample. Figure 3.8 shows the masked regions.

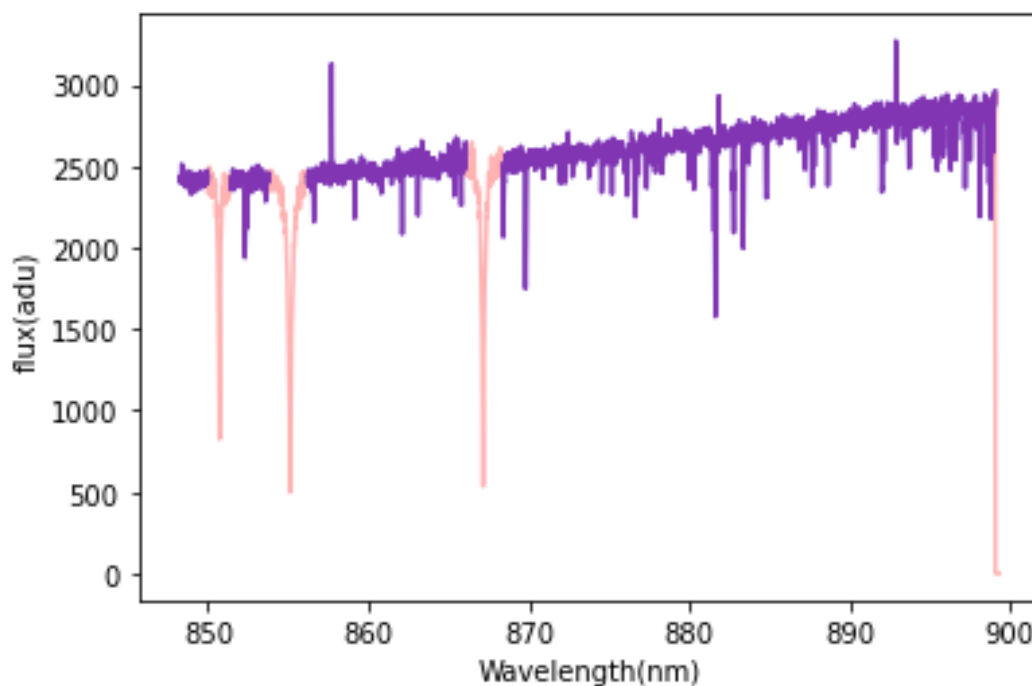


Figure 3.8: The spectrum of one of the sample stars (in purple) with masked CaT lines (in pink) and the subtraction of the median of all the sky fibres from the star spectrum. The wavelength is heliocentric corrected.

After the masking of the CaT lines, to ensure a good continuum and avoid regions that still have strong sky emission lines artifacts or strong absorption lines other than

the CaT lines, a few regions of the continuum are chosen which are 8483 Å to 8485 Å ; 8531 Å to 8533.5 Å ; 8586.5 Å to 8587.5 Å ; 8639 Å to 8640.5 Å ; 8703 Å to 8706 Å ; 8774 Å to 8775.5 Å ; 8840.5 Å to 8841.5 Å ; 8923.5 Å to 8924.5 Å ; 8960.2 Å to 8961.5 Å ; and 8982 Å to 8984 Å . It is to be noted that they do not overlap with the CaT lines which are masked as previously discussed in this section. These regions are then fitted with a 6th order polynomial (as in Wan et al., 2021) and the result for one example star in the sample is shown in Figure 3.9.

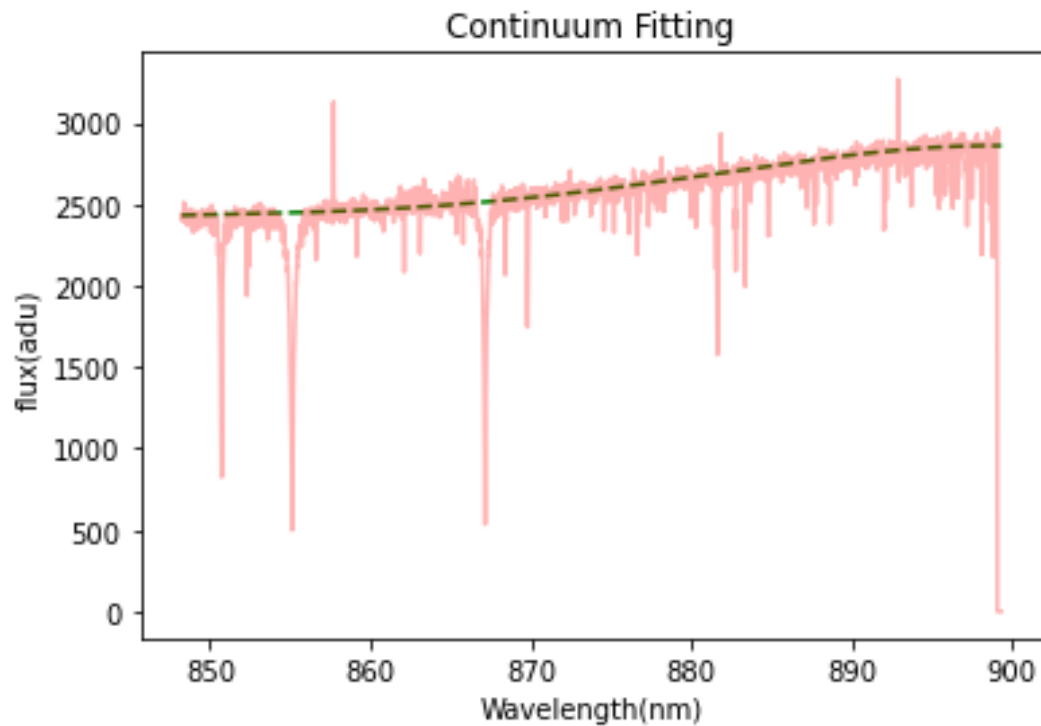


Figure 3.9: The continuum fitting of a spectrum is shown as the green dashed line. The CaT lines are masked when fitting the continuum.

The continuum is then normalized to 1 by dividing the spectrum including the CaT lines by the fitted continuum spectrum. Continuum normalization is useful when fitting the CaT lines which will be discussed in Section 3.3.

3.3 CAT LINES FITTING

The CaT absorption lines can be fitted with a Gaussian profile (Equation 3.1) but as discussed in Section 1.3, the presence of wings around the CaT lines requires a Lorentzian profile (Equation 3.2) component too. Both the Gaussian and Lorentzian profiles add up to a pseudo-Voigt profile.

$$G(\lambda) = \frac{A_g \cdot e^{-\frac{(\lambda-\lambda_0)^2}{2 \cdot \sigma_g^2}}}{\sigma_g \cdot \sqrt{2 \cdot \pi}} \quad (3.1)$$

$$L(\lambda) = \frac{A_l \cdot \sigma_l}{\pi \cdot (\lambda - \lambda_0)^2 + \sigma_l^2} \quad (3.2)$$

The shift of a spectral line compared to its rest wavelength can give the speed at which the star is moving along the line-of-sight. Using the Doppler shift Equation 1.4, the velocity can be written as in Equation 3.3. The velocity can be substituted in Equation 3.1 and Equation 3.2. giving Equation 3.4 and Equation 3.5. Since the velocity is the same for each CaT line, Equation 3.4 and Equation 3.5 describe each CaT line in terms of the star's radial velocity. The radial velocities can be used to further study the kinematic stars in the outer regions of NGC 1851.

$$v = \frac{c \cdot (\lambda - \lambda_0)}{\lambda} \quad (3.3)$$

$$G(\lambda) = \frac{A_g}{\sigma_g \cdot \sqrt{2 \cdot \pi}} \cdot e^{-\frac{(\lambda - [\lambda_0 \cdot (1 + \frac{v}{c})])^2}{2 \cdot \sigma_g^2}} \quad (3.4)$$

$$L(\lambda) = \frac{A_l \cdot \sigma_l}{\pi \cdot ([\lambda - \lambda_0 \cdot (1 + \frac{v}{c})]^2 + \sigma_l^2)} \quad (3.5)$$

$$F(\lambda) = \frac{A_g}{\sigma_g \cdot \sqrt{2 \cdot \pi}} \cdot e^{-\frac{(\lambda - [\lambda_0 \cdot (1 + \frac{v}{c})])^2}{2 \cdot \sigma_g^2}} + \frac{A_l \cdot \sigma_l}{\pi \cdot ([\lambda - \lambda_0 \cdot (1 + \frac{v}{c})]^2 + \sigma_l^2)} \quad (3.6)$$

Since the CaT lines are being fitted with a Gaussian function and a Lorentzian function, the overall function to be fitted would be a sum of the Gaussian function and the Lorentzian function as shown in Equation 3.6. Choosing the regions to be fitted with Equation 3.4 and Equation 3.5 is important so that there is no underestimation or overestimation of the equivalent widths due to other absorption lines or sky emission lines artifacts. The regions should include the CaT absorption lines as well as the wings on both sides of them. A wider region is chosen so that it encompasses the wings too and so that it considers the shift in wavelength of the CaT lines for the different stars in the sample. The regions that were chosen are: 8492 Å to 8510 Å (the region for the first CaT line); 8530 Å to 8553 Å (the region for the second CaT line); and 8662 Å to 8675 Å (the region for the third CaT line). The model fitted to these regions for each CaT line is written in Equation 3.7. The continuum needs to subtract the pseudo-Voigt profile so that the former is not included in the fitted model. The continuum is represented as the term 1 in Equation 3.7 because it was normalized to 1 as discussed in Section 3.2.

$$V(\lambda) = 1 - \left(\frac{A_g}{\sigma_g \cdot \sqrt{2 \cdot \pi}} \cdot e^{-\frac{(\lambda - [\lambda_0 \cdot (1 + \frac{v}{c})])^2}{2 \cdot \sigma_g^2}} + \frac{A_l \cdot \sigma_l}{\pi \cdot ([\lambda - \lambda_0 \cdot (1 + \frac{v}{c})]^2 + \sigma_l^2)} \right) \quad (3.7)$$

$$\begin{aligned}
A(\lambda) &= \frac{A_{g1}}{\sigma_{g1} \cdot \sqrt{2} \cdot \pi} \cdot e^{-\frac{(\lambda - [\lambda_0 \cdot (1 + \frac{v}{c})])^2}{2 \cdot \sigma_{g1}^2}} + \frac{A_{l1} \cdot \sigma_{l1}}{\pi \cdot ([\lambda - \lambda_0 \cdot (1 + \frac{v}{c})]^2 + \sigma_{l1}^2)} \\
B(\lambda) &= \frac{A_{g2}}{\sigma_{g2} \cdot \sqrt{2} \cdot \pi} \cdot e^{-\frac{(\lambda - [\lambda_0 \cdot (1 + \frac{v}{c})])^2}{2 \cdot \sigma_{g2}^2}} + \frac{A_{l2} \cdot \sigma_{l2}}{\pi \cdot ([\lambda - \lambda_0 \cdot (1 + \frac{v}{c})]^2 + \sigma_{l2}^2)} \\
C(\lambda) &= \frac{A_{g3}}{\sigma_{g3} \cdot \sqrt{2} \cdot \pi} \cdot e^{-\frac{(\lambda - [\lambda_0 \cdot (1 + \frac{v}{c})])^2}{2 \cdot \sigma_{g3}^2}} + \frac{A_{l3} \cdot \sigma_{l3}}{\pi \cdot ([\lambda - \lambda_0 \cdot (1 + \frac{v}{c})]^2 + \sigma_{l3}^2)} \\
V_{CaT}(\lambda) &= 1 - (A(\lambda) + B(\lambda) + C(\lambda)),
\end{aligned} \tag{3.8}$$

where $A(\lambda)$, $B(\lambda)$ and $C(\lambda)$ are the fitted profiles for each CaT and $V_{CaT}(\lambda)$ is the pseudo-Voigt profile of all three CaT lines.

Equation 3.7 for the profile assumes positive values for A_g and A_l for an absorption line. Equation 3.8 which is the profile for the three CaT lines together, is fitted for these regions using a Markov chain Monte Carlo (MCMC) method that takes into account uncertainties on the flux values. The python package *emcee* is used (Foreman-Mackey et al. 2013). Also fitting through this method allows the estimation of optimum values of parameters with their uncertainties. The parameters to be estimated are A_l , A_g , σ_l , σ_g for each line, and v (common to all three lines) from Equation 3.8. The MCMC method explores parameter space until the optimal model and its parameters are reached. For this thesis, the number of steps of the MCMC chain for the model described in Equation 3.8 is 3000 and the equilibrium distribution of samples in the MCMC chain is reached after 1500 steps so this "burn-in" phase of 1500 steps is removed from the chain in the estimation of the optimal parameters. The best-fitting value and 1σ uncertainties of each parameter are extracted from the MCMC chain for each parameter. Figure 3.3 shows the CaT lines fitting for one star

in the sample.

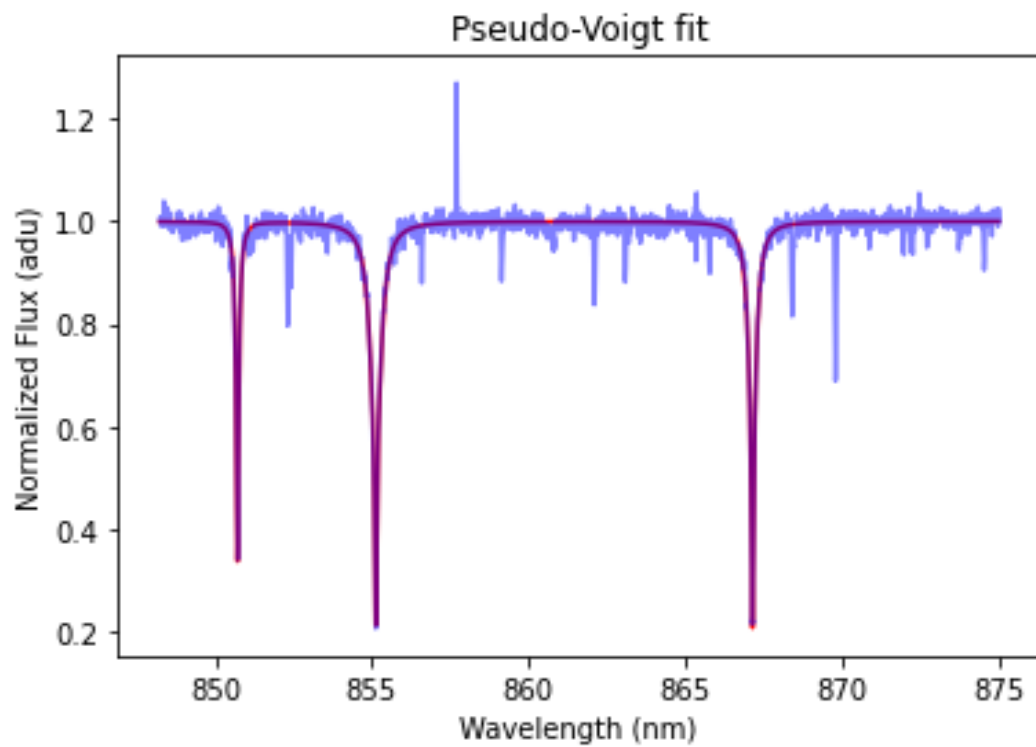


Figure 3.10: Fit of the CaT lines with a pseudo-Voigt profile for one of the sample stars.

The pseudo-Voigt model for 14 stars did not give proper optimum parameters and this ended up poorly fitting the CaT lines, so they were excluded from the analysis. Figure 3.11 shows the pseudo-Voigt profile fitted for one of those stars and the problem can be seen in how the peak of the fitted model does not match the CaT spectral lines. These stars require a better fitting profile which will allow a better estimation of the amplitude and the equivalent width of the CaT lines.

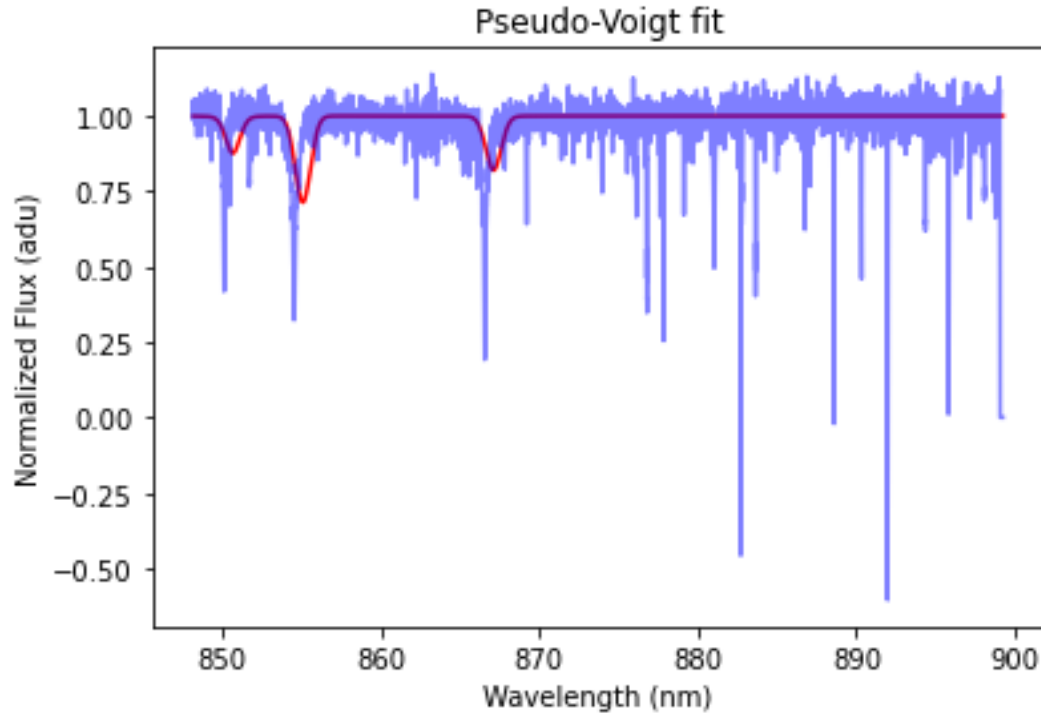


Figure 3.11: The poorly fitted pseudo-Voigt profile for a star using MCMC.

3.4 EQUIVALENT WIDTHS

The equivalent width is the area between the absorption line and the continuum as discussed in Section 1.3. The equivalent width is derived as shown below and it requires the amplitude parameters A_l and A_g of each CaT absorption line. The equivalent width is the integrated area between the CaT line and the continuum. To find the equivalent width, the area under the CaT is integrated first by the following procedures.

The function to fit one CaT line is:

$$F(\lambda) = 1 - \left(\frac{A_g \cdot e^{-\frac{(\lambda-\lambda_0)^2}{2\sigma_g^2}}}{\sigma_g \cdot \sqrt{2 \cdot \pi}} + \frac{A_l \cdot \sigma_l}{\pi \cdot (\lambda - \lambda_0)^2 + \sigma_l^2} \right) \quad (3.9)$$

To find the equivalent width, the integral of the above profile is done:

$$I = \int_{\lambda_A}^{\lambda_B} 1 - \left(\frac{A_g \cdot e^{-\frac{(\lambda-\lambda_0)^2}{2\cdot\sigma_g^2}}}{\sigma_g \cdot \sqrt{2\cdot\pi}} + \frac{A_l \cdot \sigma_l}{\pi \cdot (\lambda - \lambda_0)^2 + \sigma_l^2} \right) d\lambda, \quad (3.10)$$

where

$$\lambda_A = 0 \quad (3.11)$$

$$\lambda_B = \infty.$$

Therefore:

$$I = (\lambda_B - \lambda_A) - A_g - A_l \quad (3.12)$$

To get the equivalent width, the area I must be subtracted from the area under the continuum. Therefore:

$$(\lambda_B - \lambda_A) - I = (\lambda_B - \lambda_A) - (\lambda_B - \lambda_A) + A_g + A_l = EW \quad (3.13)$$

$$EW = A_g + A_l.$$

Equation 3.13 gives the equivalent width for one CaT line. To get the total equivalent width of the three CaT lines, the sum of the amplitude parameters of the three CaT lines can be calculated.

For this paper, the total equivalent width, ΣCa is the sum of the equivalent width for the two strongest CaT line. The parameters derived by the MCMC method to fit the model in Equation 3.7 for each CaT line, are used to find ΣCa as described in Equation 3.13.

From the best-fitting model parameters and uncertainties on each of the model

parameters estimated using MCMC, we can find ΣCa and its uncertainties.

Since each star was observed two times, the average ΣCa for each star is calculated from the ΣCa obtained from each of its observations. The uncertainties on ΣCa are slightly asymmetric so the normal propagation of error as described by Equation 3.14 cannot be done in practice. However, since the $+1\sigma$ and -1σ uncertainties are similar, an average of the lower uncertainty and the higher uncertainty for ΣCa is calculated for each observation. To find the uncertainty on the averaged ΣCa , the averaged uncertainty for the ΣCa for each observation is propagated by using Equation 3.14.

$$\sigma_f = \sqrt{\left(\frac{\delta f}{\delta A} \cdot \sigma_B\right)^2 + \left(\frac{\delta f}{\delta B} \cdot \sigma_A\right)^2} \quad (3.14)$$

where σ_f is the uncertainty in a function, A and B are variables of the function f, σ_A and σ_B are uncertainties in A and B respectively for $f = A + B$.

The visual magnitude, V of each star observed is provided with the calibrated data. Since the averaged ΣCa was found by considering ΣCa of each observation of the same star, this reduced the 53 to 56 observations for each observing block as mentioned in Section 3.1 to a total of 107 stars observed throughout the four observing blocks that have a total of 214 observations (excluding the poorly fitted CaT lines spectra) which is double the number of stars because each star target was observed twice.

Chapter 4

Results of the Spectroscopic Analysis

4.1 THE METALLICITY DISTRIBUTION

As described Equation 1.2, the relationship between the equivalent width is non-linear to the magnitude. This relationship will give the reduced equivalent width which will be used in Equation 1.3 which is the non-linear metallicity scale and it accounts for stars fainter than the horizontal branch. It is being used in this thesis because most of the stars from the sample are fainter than the horizontal branch. The value of $V_{HB}(16.09)$ for the cluster NGC 1851 (Harris,1986, revised 2010) is used to find the reduced equivalent width and to correct for the temperature and $\log(g)$ which can affect the metallicity as described in 1.3.

Among the stars in the sample, 4 stars were removed from the analysis because their line-of sight velocity was very different from that of the cluster. Figure 4.1 shows the metallicity distribution of the remaining 89 stars.

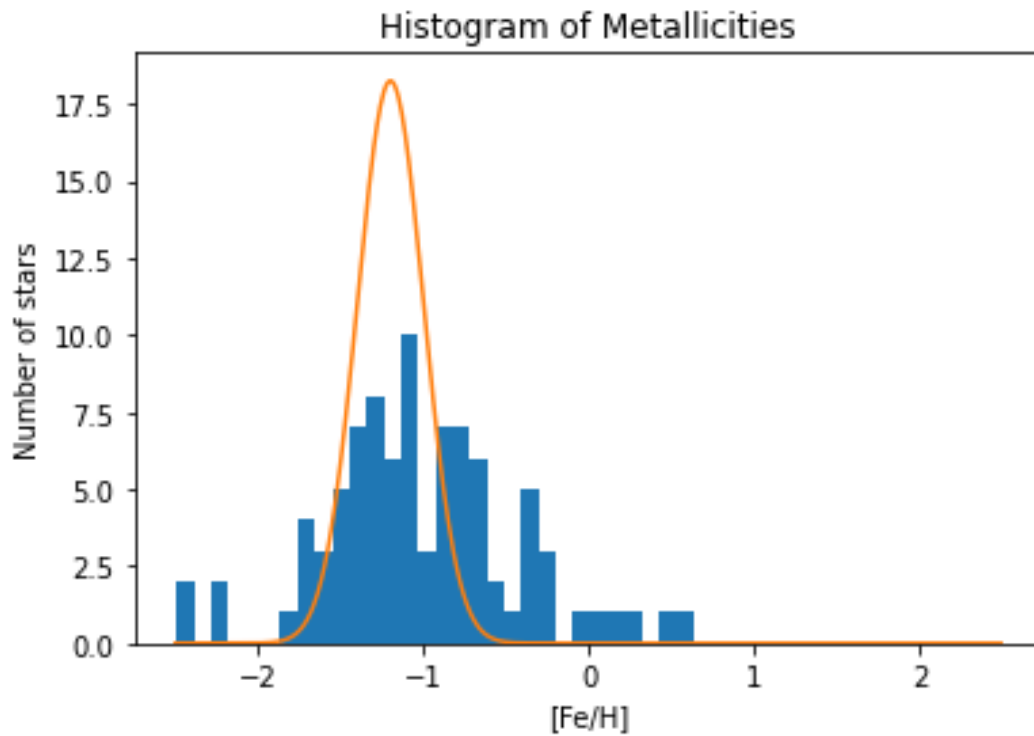


Figure 4.1: The metallicity distribution of the stars in the outskirts of NGC 1851 studied in this thesis (blue histogram). The orange Gaussian distribution represents the $[\text{Fe}/\text{H}]$ distribution if the stars had no significant metallicity spread and the same metallicity as the stars in the centre of the cluster.

Chapter 5

Discussion and Conclusion

5.1 THE SPREAD IN METALLICITY

Figure 4.1 shows the metallicity distribution of the stars from the sample. The Gaussian distribution (orange) which is overplotted in Figure 4.1 has a mean value at $[\text{Fe}/\text{H}] = -1.2$ dex and standard deviation of 0.2 dex. The metallicity distribution obtained for the stars appears to have multiple peaks within the mean value of the Gaussian distribution. The structure and multiple peaks in the histogram may be a result of the limited number of stars analysed (there is a limited number of bright stars in the outskirts of the cluster). We can check if the observed spread in the metallicity distribution is consistent with a single metallicity within errors. To find the uncertainty on the metallicity, the uncertainty of the reduced equivalent width needs to be found. Using propagation of errors, the errors in reduced equivalent width is equal to the error in equivalent width ($\sigma W' = \sigma \Sigma \text{Ca}$) and the errors in metallicity in found by using Equation 5.1. A typical uncertainty of around 0.2 dex is inferred.

$$\sigma_{[\text{Fe}/\text{H}]} = \sqrt{\left(0.04 \cdot \sigma W'\right)^2 + \left(0.07 \cdot 2 \cdot \sigma W'\right)^2} \quad (5.1)$$

Some of the stars have a metallicity consistent with $[\text{Fe}/\text{H}] = -1.2$ within the errors but there are some which have higher $[\text{Fe}/\text{H}]$ values and are not found within

uncertainties. However, due to the larger amount of stars found within the Gaussian curve, it can be said that NGC 1851 might not have been in a progenitor dwarf galaxy where its stellar halo stars would originate.

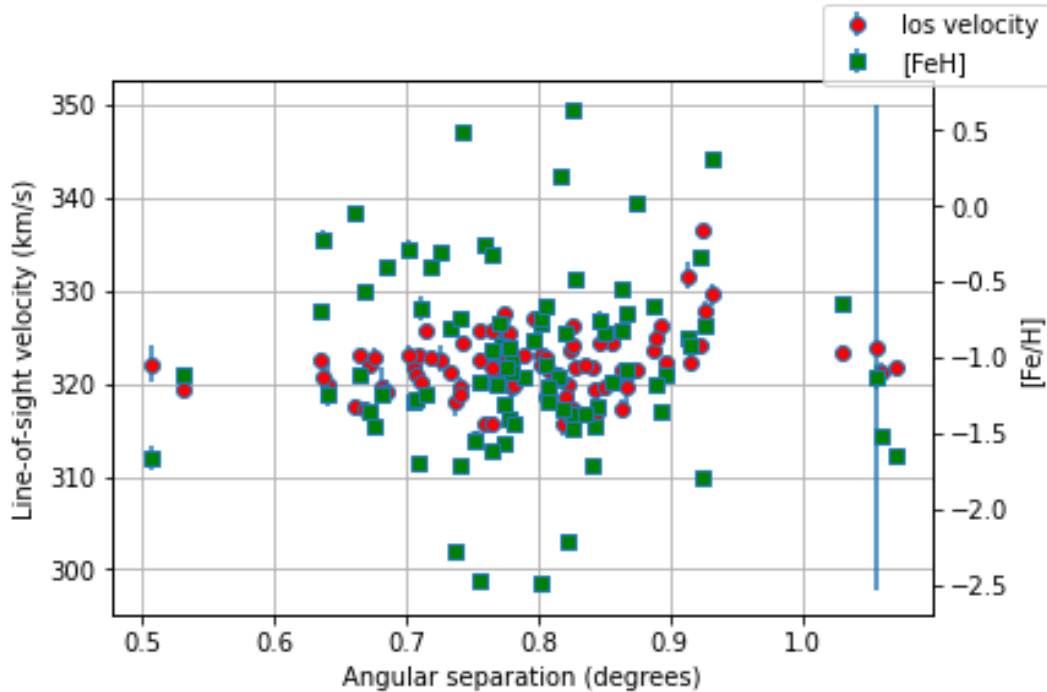


Figure 5.1: The line-of-sight velocity distribution with $[\text{Fe}/\text{H}]$ of the stars.

Figure 3.3 shows the line-of-sight velocity and $[\text{Fe}/\text{H}]$ distributions with angular distance from the centre of the cluster. The line-of-sight velocity distribution can help in further filtering stars for the cluster because stars with line-of-sight different from that of the cluster within errors, can be removed from the analysis. One star was removed from the metallicity analysis because it had a significantly large line-of-sight velocity compared to that of the cluster.

The small spread in $[\text{Fe}/\text{H}]$ and the line-of-sight velocity similar to that of the cluster may suggest that NGC 1851 was not part of a progenitor dwarf galaxy. The values of $[\text{Fe}/\text{H}]$ can be cross-checked with other studies that observed a few stars

in common with our sample so that the metallicity values and spread can be further studied. Also, the stars that have metallicities that are not within the Gaussian distribution can be more studied so that their metallicities can be explained.

Bibliography

- Armandroff, T. E., & Da Costa, G. S. 1991, *AJ*, 101, 1329
- Harris W.E. *AJ*, 112, 1487 the Catalog of Parameters for Milky Way Globular Clusters, website: <http://physwww.mcmaster.ca/harris/mwgc.ref>
- Bekki, K., & Freeman, K. C. 2003, *MNRAS*, 346, 11
- Bekki, K., & Yong, D. 2012, *MNRAS*, 419, 2063
- Brodie, J. P., & Strader, J. 2006, *ARA&A*, 44, 193
- Carballo-Bello, J. A., et al. 2012, *MNRAS*, 419, 14
- Carrera, R., et al. 2007, *AJ*, 134, 1298
- Carrera, R., et al. 2013, *MNRAS*, 434, 1681
- Carretta, E., & Gratton, R. G. 1997, *A&AS*, 121, 95
- Gallagher, J. S., et al. 1994, *PASP*, 106, 1225
- Han, S. I., et al. 2009, *ApJ*, 707, 190
- Husser, T. O., et al. 2020, *A&A*, 635, 114
- King, I. 1962, *AJ*, 67, 274
- Kraft, R. P., & Ivans, I. I. 2003, *PASP*, 115, 143
- Kundu, A., & Whitmore, B. C. 1998, *AJ*, 116, 2841
- Marino, A. F., et al. 2014, *MNRAS*, 442, 3044
- McConnachie, A. 2011, *AJ*, 144, 4M
- Mercado, F. J., et al. 2021, *MNRAS*, 501, 5121
- Olszewski, E. W., et al. 2009, *AJ*, 138, 1570
- Rusakov, V., et al. 2021, *MNRAS.tmp*, 57R
- Rutledge, G. A., et al. 1997, *PASP*, 109, 907
- Sollima, A., et al. 2012, *MNRAS*, 426, 1137
- Wan, Z., et al. 2021, *MNRAS*, 502, 4513
- Zinn, R., & West, M. J. 1984, *AJ*, 55,45